

Tufan Arslan

Department of Marine Technology,
Norwegian University of Science
and Technology,
Trondheim 7491, Norway
e-mail: tufan.arslan@ntnu.no

Stefano Malavasi

Department of Civil and Environmental
Engineering, Politecnico di Milano,
Milan 20133, Italy
e-mail: stefano.malavasi@polimi.it

Bjørnar Pettersen

Department of Marine Technology,
Norwegian University of Science
and Technology,
Trondheim 7491, Norway
e-mail: bjornar.pettersen@ntnu.no

Helge I. Andersson

Department of Energy and Process Engineering,
Norwegian University of Science
and Technology,
Trondheim 7491, Norway
e-mail: helge.i.andersson@ntnu.no

Turbulent Flow Around a Semi-Submerged Rectangular Cylinder

The present work is motivated by phenomena occurring in the flow field around structures partly submerged in water. A three-dimensional (3D) unsteady flow around a rectangular cylinder is studied for four different submergence ratios by using computational fluid dynamics (CFD) tools with the large eddy simulation (LES) turbulence model. The simulation results are compared to particle image velocimetry (PIV) measurements at the Reynolds number $Re = 12,100$ and the Froude number $Fr = 0.26$. The focus in our investigation is on the characterization of the behavior of vortex structures generated by separated flow. Another target in the study is to obtain a better knowledge of the hydrodynamic forces acting on a semi-submerged structure. The computed force coefficients are compared with experimental measurements. [DOI: 10.1115/1.4025144]

Keywords: LES, bluff body, free surface, numerical simulation, PIV

Introduction

Bluff body hydro- and aerodynamics have many applications in several industrial fields such as flow around bridge decks, large buildings, floating offshore structures, and cooling towers. Despite the simple body geometry, the flow field around a rectangular cylinder is very complex, even at low Reynolds numbers. This flow is even more complex when a semi-submerged structure is considered. Classical unsteady Reynolds-averaged Navier–Stokes (URANS) solvers give a rough description of the unsteadiness of the flow and are limited to dominant low frequencies. They generally fail to estimate such flows well, mainly due to an inaccurate prediction of eddy-viscosity. Reynolds stress models provide a more appropriate level of modeling but they are still unsatisfactory. Turbulent flows at low Reynolds numbers may be predicted by direct numerical simulation (DNS), where even the smallest length and time scales of turbulence are resolved without introducing any turbulence model. In high Reynolds number flows, DNS is not feasible. On the contrary, large eddy simulation (LES) models resolve a wide range of turbulence scales and are affordable in many realistic applications. Another reason for the focus on the LES for modeling flow around a bluff body is related to the rather poor results obtained when using the URANS equations based on the statistical turbulence models. This is probably due to the challenges such as massive flow separation and reattachment, streamline curvature, transition from laminar to turbulent regime, interaction between large and small turbulent scales, recirculation and secondary flows, vortex shedding, and the existence of inherent 3D flow structures.

The flow around a fully submerged rectangular cylinder has been investigated by many researchers in previous years. Experimental work has been done in wind tunnels or water channels to determine aerodynamics, loads, and vortex shedding frequencies in its wakes by Norberg [1], Awbi [2], Deniz and Staubli [3], Kim

et al. [4], Matsumoto et al. [5], Mills et al. [6], Nakamura and Yoshimura [7], Shadaram et al. [8], Nakamura and Ohya [9], Nakaguchi et al. [10], and Washizu et al. [11]. Some researchers combined measurements with flow visualizations to provide information about flow structures near the solid body; see, e.g., Okajima [12]. In particular, Knisely [13] reviewed and summarized the characteristics of the Strouhal numbers of rectangular cylinders at different angles of incidence. Bearman and Trueman [14] presented the measurements of the base pressure coefficient, drag coefficient, and Strouhal number of rectangular cylinders in their paper. Malavasi and Blois [15] provided the mean flow field characterization around a rectangular cylinder using topological parameters and used these parameters to study the effects of the boundary conditions on the mean flow structure.

Hemon and Santi [16] investigated the flow around an elongated rectangular and a square cylinder, both experimentally and numerically. Kuroda et al. [17] performed the LES and compared the results with particle image velocimetry (PIV) data. Numerical simulations of such flows were earlier restricted to two dimensions (2D) because of the high level of complexity, as in Davis et al. [18], Kondo and Yamada [19], Ohya et al. [20], and Sohankar et al. [21]. The flow around a rectangular section with an aspect ratio of 4:1 at the Reynolds number 10^5 is calculated by Yu and Kareem [22]. Shimada and Ishihara [23] made 2D calculations for the flow around rectangular sections with different aspect ratios (from 0.6:1 to 8:1). Nakamura et al. [24] investigated vortex shedding from elongated cylinders, both numerically and experimentally (aspect ratio from 1:1 to 5:1). Tamura and Ito [25] simulated the aerodynamic characteristics of various rectangular sections by employing higher order schemes. In recent years, an improvement in the computational capacity makes 3D simulations feasible, as shown by Hirano et al. [26], Krajnovic and Davidson [27], Lam et al. [28], Sohankar [29], Almeida et al. [30], Noda and Nakayama [31], and Arslan et al. [32].

The benchmark on the aerodynamics of a 5:1 rectangular cylinder (BARC) has been proposed by Bartoli et al. [33] to create a benchmark database for flow around a rectangular cylinder. Among the contributors to this benchmark, 3D flow features and

Contributed by the Ocean, Offshore, and Arctic Engineering Division of ASME for publication in the JOURNAL OF OFFSHORE MECHANICS AND ARCTIC ENGINEERING. Manuscript received March 27, 2012; final manuscript received July 10, 2013; published online September 27, 2013. Assoc. Editor: Sergio H. Sphaier.

force coefficients are numerically investigated by Bruno et al. [34]. Mannini and Schewe [35] performed 3D URANS and DES simulations and showed the separated flow around the rectangular section with an aspect ratio of 5:1. Experimental work has been done to measure the aerodynamic forces for the BARC benchmark case over a wide range of Reynolds numbers by Schewe [36,37].

While there are only a few references in the literature regarding the semi-submerged case, Arslan et al. [38] numerically investigated the flow around a rectangular section on the water surface by using the LES model. The flow around a rectangular section with the free surface effects included is also of interest in other applications; for example for a bridge section during a critical river flood event. The bridge may then become partly or completely submerged by the river flow. Malavasi and Guadagnini [39] investigated the effect of the free surface on the flow around a submerged rectangular cylinder mounted near the water surface and provided experimental data for the mean force on the body at different submersion ratios. The PIV technique is also used to visualize the flow field around a partly submerged rectangular bridge deck by Malavasi et al. [40] and Malavasi and Blois [41]. Experiments have been conducted to investigate the flow separation effects induced by water waves traveling over a submerged rectangular obstacle by Ting and Kim [42].

Mathematical Formulation

Flow Model and Numerical Solution Procedure. The governing equations solved in the LES modeling are a set of filtered Navier–Stokes equations describing the two phases (gas and liquid) and their mixture. In this case, the gas phase is air and the liquid phase is water. The filtered N–S equations can be written as

$$\frac{\delta \bar{p}}{\delta t} + \frac{\delta}{\delta x_j} (\bar{p} \bar{u}_{ij}) = 0 \quad (1)$$

and

$$\frac{\delta}{\delta t} (\bar{\rho} \bar{u}_i) + \frac{\delta}{\delta x_j} (\bar{\rho} \bar{u}_i \bar{u}_j) = -\frac{\delta \bar{P}}{\delta x_i} + \frac{\delta}{\delta x_j} \left\{ \mu \left(\frac{\delta \bar{u}_i}{\delta x_j} \right) - \tau_{ij} \right\} \quad (2)$$

where the overbar points out the filtering operation. The pressure is defined as $P = P_s + \rho g y$ where P_s is the static pressure and $\rho g y$ is the hydrostatic component of the pressure in water. Here, τ_{ij} is the subgrid-scale turbulent stress defined by

$$\tau_{ij} \equiv \bar{\rho} (\bar{u}_i \bar{u}_j - \bar{u}_i \bar{u}_j) \quad (3)$$

and needs to be modeled. The subgrid-scale turbulence is modeled using the dynamic Smagorinsky model. In the original eddy-viscosity model proposed by Smagorinsky [43], the subgrid-scale stresses are modeled using

$$\tau_{ij} - \frac{1}{3} \delta_{ij} \tau_{kk} = -2 \bar{\rho} C \bar{\Delta}^2 |\bar{S}| \bar{S}_{ij} \quad (4)$$

where C is the model coefficient ($C = 0.1 \sim 0.2$), S_{ij} is the resolved rate-of-strain tensor, $|\bar{S}| = \sqrt{2 \bar{S}_{ij} \bar{S}_{ij}}$ is its modulus, and $\bar{\Delta} \equiv V^{1/3}$, where V is the volume of the cell. In the dynamic procedure, the model coefficient C is computed during the LES simulation on-the-fly. Details of the procedure can be found in Germano et al. [44].

The presence of two phases is modeled by a free surface capture method, the volume of fluid (VOF) method, proposed by Hirt and Nichols [45]. In this method, the volume fraction (α) in the two-phase flow can vary from 0 to 1 and is obtained from a transport equation

$$\frac{\delta \alpha}{\delta t} + \frac{\delta}{\delta x_j} (\alpha \bar{u}_j) = 0 \quad (5)$$

The density and viscosity of the fluid mixture are computed as functions of α

$$\begin{aligned} \rho &= (1 - \alpha) \rho_w + \alpha \rho_a \\ \mu &= (1 - \alpha) \mu_w + \alpha \mu_a \end{aligned} \quad (6)$$

where the subscripts “a” and “w” indicate air and water, respectively.

The simulations are performed by the ANSYS-Fluent software. Fluent employs a cell-centered finite-volume method that permits the use of polyhedral cells. Higher order methods are used for the discretization of the N–S and VOF equations. In order to ensure accuracy, efficiency, and stability, bounded central-differencing is adopted to solve the filtered momentum equations. This is a non-dissipative second-order-accurate scheme combined with a non-linear flux-limiter to suppress numerical oscillations. A high resolution interface-capturing scheme by Muzaferija et al. [46] is employed to resolve sharp interfaces. For pressure-velocity coupling, the PISO algorithm is used. The temporal discretization in the segregated solvers employs a fully implicit three-level second-order accurate scheme. The discretized equation system is solved using the point-wise Gauss–Seidel iterative algorithm with an acceleration of an algebraic multigrid method. More details can be found in Kim [47].

Computational Domain, Grid, and Boundary Conditions.

Figure 1 shows the definition of the problem and the geometric parameters. The length of the rectangular cylinder is $l = 3s$, where “s” is the total height of the rectangular cylinder. The distance between the cylinder and water floor is h_b and h_M is the water depth. The submergence ratio (h^*) is defined as the draft of the cylinder ($T = h_M - h_b$) to the total height of the cylinder (s), i.e., $h^* = T/s$. Simulations are performed for $h^* = 0.2, 0.4, 0.6$, and 0.8 . The incoming flow velocity U_0 corresponds to the Reynolds number 12,100 ($Re = U_0 s / \nu$) and the Froude number 0.26 ($Fr = U_0 / (g s)^{0.5}$). The turbulence intensity of the incoming flow is set to 14% (which is a high value), matching the turbulence level measured in the circulation tunnel.

The entire 3D computational domain and boundaries can be seen in Fig. 2. The inlet and outlet are a distance $10s$ and $30s$ away from the rectangular section’s front and back surfaces, respectively. The length of the cylinder in the spanwise direction is $d = 8.33s$. This is chosen to be consistent with the experimental setup, which will be described in the next section. The distance h_b from the cylinder bottom surface to the lower boundary surface is $2.33s$, which exactly matches the experimental conditions. Thus, blockage effects can be considered in the simulations. The upper boundary (in the air domain) is located $4s$ from the top surface of the cylinder.

The boundary conditions at the inlet and outlet side have two parts: At the part of the inlet surface where water is coming in, a uniform velocity is applied, based on the relevant Reynolds number. At this surface the air volume fraction α is 0. The water level at the inlet boundary also varies for different submergence ratios. At the lower part of the outlet surface where the water is leaving, we apply hydrostatic pressure ($-\rho g y$), based on the vertical

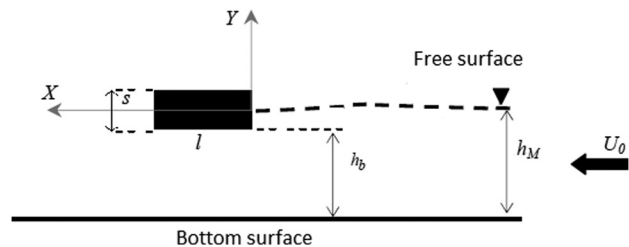


Fig. 1 Sketch of the geometric parameters

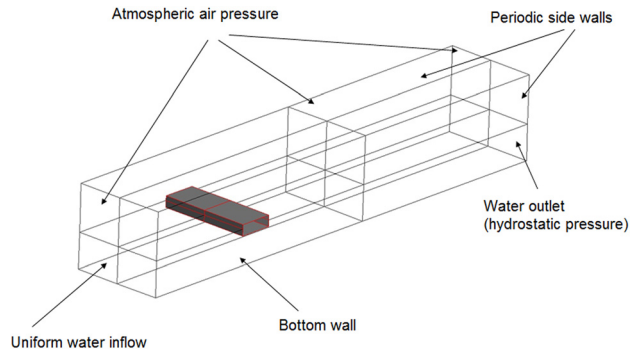


Fig. 2 The 3D computational domain with boundary surfaces and its boundary conditions

distance from the free water surface. Simulations are performed with periodic conditions at the side walls for all h^* values. The bottom surface is considered as a no-slip wall. Zero atmospheric pressure is applied at the rest of the surface and on the upper surface of the air domain, as seen in Fig. 2.

To discretize the computational domain several different meshes with different resolutions, have been used. For each mesh, a hexagonal type grid which has an unstructured topology in the streamwise and vertical direction (xy plane) is used, as shown in Fig. 3. The grid is structured in the spanwise (z) direction. Near the cylinder, at its wet bottom wall and at the free surface, structured grid layers are used in order to have a sufficient mesh size and quality inside the boundary layers and water-air interfaces. The number of the structured layers in this region is 15 for the cylinder and 20 for the bottom. The first grid spacing near the wall is $0.0003 s$ and $0.0016 s$ for the cylinder and bottom surfaces, respectively. The grid expands out from the surface with the ratio equal to 1.2. The structured mesh region at the water-air interface has a total of 12 layers expanding into both the air and water sides with a ratio of 1.2 by starting with a thickness of $0.005 s$ for the first layer. These parameters have been set equal for all meshes that are used in the simulations. Outside of the hexahedral layer the quadrilateral elements in the xy plane expand with the ratio 1.15 and reach different maximum sizes. The maximum element sizes near the outer boundaries are tabulated in Table 1. This expansion is controlled in the wake region and close to the lower part of the cylinder, which is called "refinement region" (see Fig. 3). For MESH-1 the grid size is kept between $0.025 s$ – $0.040 s$ in this area, as shown in Table 1. The mesh on the air side is rather coarse (maximum $0.33 s$) for each computational grid because detailed

air flow structures are not of interest in this work, except for very close to the water-air interface. The total number of elements in the xy plane is around 47,500 and 150×70 elements are used for discretizing the surface of the rectangular section with clustering towards the corners. For MESH-2, 300×75 elements have been used for the rectangular section in the xy plane and the total number of elements in this plane is around 112,500 for this grid. The element size in the spanwise direction is constant $0.21 s$ (40 elements in the z direction). This brings the total number of three-dimensional hexagonal elements to about 1.9×10^6 for MESH-1 and 4.5×10^6 for MESH-2. The number of elements in the xy plane and in total, the average grid sizes in the refinement region, and the outer boundaries, element numbers on the cylinder surface, and spanwise directions are shown in Table 1 for MESH-3, MESH-4, MESH-5, and MESH-6. The resulting y^+ values are below 0.56 on the cylinder surface and the maximum value of the y^+ is around 1 at the bottom wall surface for all meshes which have the same resolution and topology in the structural layers near the wall.

The time is nondimensionalized by the uniform inlet velocity (U_0) and height s as $\tau = t U_0 / s$ and the simulations are carried out for $\tau = 330$ in order to reach statistical convergence. The first 60 nondimensional time units are discarded in the calculation of the average RMS values of the velocity fields and force coefficients. The remaining simulation time (270 time units) corresponds to approximately 80 vortex shedding cycles. The nondimensional time increment is roughly 0.003 (0.001 s). The Strouhal number $St = fs / U_0$, where f is the frequency, is gathered from the lift coefficient as a result of the FFT analysis. Mean drag and lift coefficients are calculated from instantaneous forces for each time step and nondimensionalized based on the draft and the length of the rectangular cylinder (T and l), the free stream velocity (U_0), and the spanwise length of the cylinder (d) in the simulations

$$C_D = \frac{F_D}{0.5 \rho U_0^2 T d} \quad (7)$$

$$C_L = \frac{F_L}{0.5 \rho U_0^2 l d}$$

Experimental Setup

The experiments were performed in a 5 m long Plexiglas laboratory flume with a 0.5 m wide and 0.6 m high cross section. The flow rate and water level were regulated by an inlet valve. The free stream turbulence intensity for the incoming water is 14%. The rectangular cylinder is fixed to the channel side-walls at a distance of 3.35 m from the inlet section and a distance of

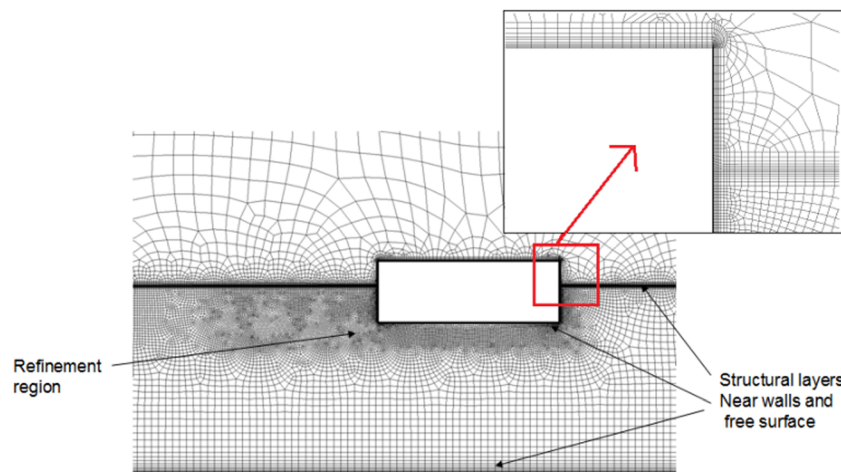


Fig. 3 Cross section of the 3D computational mesh (MESH-1) showing details at the corner (upper right)

Table 1 Mesh sizes and distribution

Case number	Mesh (million)	Mesh xy plane	Spanwise cells	On the cylinder	Refinement region	Outer domain
MESH-1	1.9	47,500	40	150×70	$0.025\text{--}0.04\text{ s}$	$0.12\text{--}0.17\text{ s}$
MESH-2	4.5	112,500	40	300×75	$0.01\text{--}0.02\text{ s}$	$0.12\text{--}0.17\text{ s}$
MESH-3	9.0	225,000	40	100×600	$0.007\text{--}0.01\text{ s}$	$0.08\text{--}0.15\text{ s}$
MESH-4	20.0	500,000	40	120×720	$0.004\text{--}0.007\text{ s}$	$0.06\text{--}0.12\text{ s}$
MESH-5	3.2	47,500	68	150×70	$0.025\text{--}0.04\text{ s}$	$0.12\text{--}0.17\text{ s}$
MESH-6	3.8	47,500	80	150×70	$0.025\text{--}0.04\text{ s}$	$0.12\text{--}0.17\text{ s}$

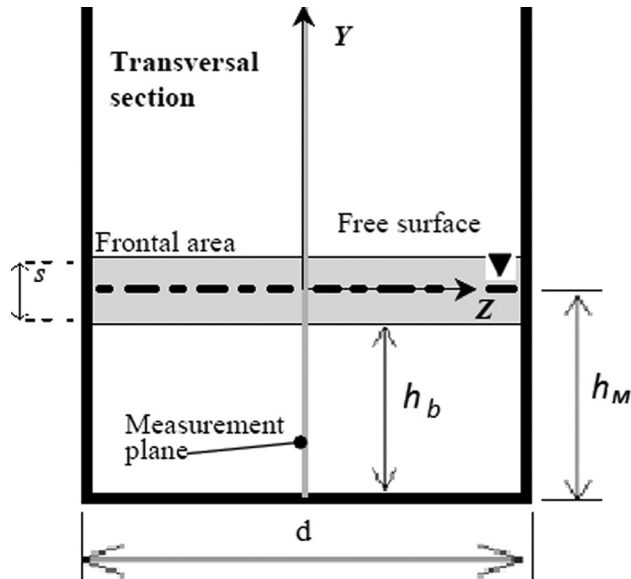


Fig. 4 Cross section of the experimental setup and measurement plane for the PIV data shown

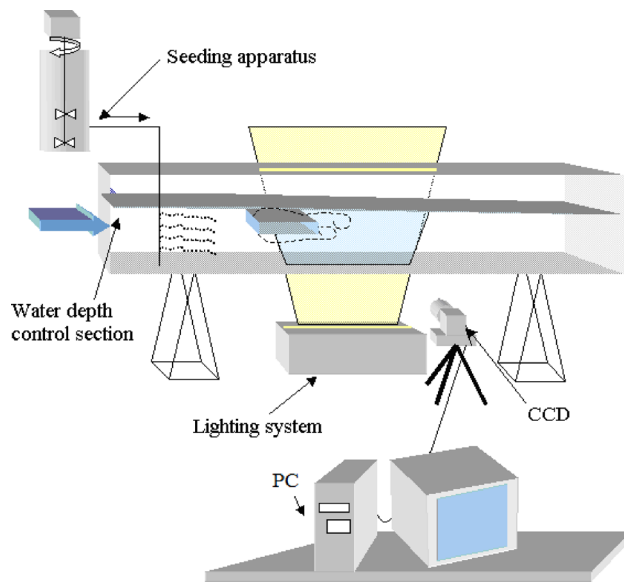


Fig. 5 The PIV measuring setup

$h_b = 0.14\text{ m}$ from the channel floor, as seen in Fig. 1. The transverse section of the flume is illustrated in Fig. 4. The spanwise length (d) of the physical model is 0.5 m ; its length and height are $l = 0.18\text{ m}$ and $s = 0.06\text{ m}$ in the x and y direction, respectively. The direct measurement of forces was performed using a pair of dynamometers. Detailed information about the experimental

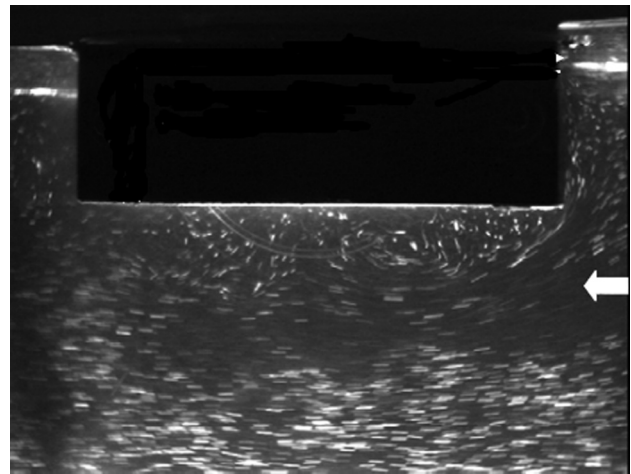


Fig. 6 A single image of the seeded flow from the measurement plane [40]

apparatus and method for measuring forces can be found in Malavasi and Guadagnini [39].

A time resolved PIV (particle image velocimetry) technique was used to measure 2D velocity fields. The PIV apparatus is composed of an optical fiber conveying a 150 W laser light source, a particle dispenser, a progressive scan camera, and a computer mounted near the wall of the circulation tunnel. Figure 5 shows the PIV acquisition apparatus in general.

The seeding apparatus seeds the flow with white polystyrene particles with a diameter of $400\text{ }\mu\text{m}$ and a density of $\rho = 1050\text{ kg/m}^3$, which is close to that of water. The lighting system creates a light sheet of thickness 0.005 m in the flow at the mid-section of the circulation tunnel. Images of the illuminated polystyrene particles were captured by using a charged coupling device (CCD) video camera. It allows one to grab pictures with a maximum frame rate of $f = 50\text{ Hz}$ and a pixel resolution of (x - y) 763×576 . The acquisition time of the sequences was limited by the storage capacity of the computer. The available acquisition system configuration allowed us to allocate 1600 image buffers that correspond to 32 s of acquisition. Figure 6 shows an example of an analyzed time frame in which the trajectories of the running particles are visible. The length of each trajectory, naturally, is due to the corresponding instantaneous velocity and to the shutter time of the video camera. An exposure time of 0.02 s was used. More detailed information about the PIV equipment setup can be found in Ref. [41].

In the experiments, the forces are measured by means of a pair of *ad hoc* insulated dynamometers. The physical model is subdivided into three parts, as seen in Fig. 7 (right). Only the middle portion of the cylinder, which is 0.25 m wide and labeled as the "sensitive part," is taken into account for force measurements to avoid the wall effects.

According to the experimental setup for the force measurements, the drag and lift coefficients are calculated based on the length of this sensitive part ($d/2$), height of the rectangular cylinder (s), and free stream velocity (U_0)

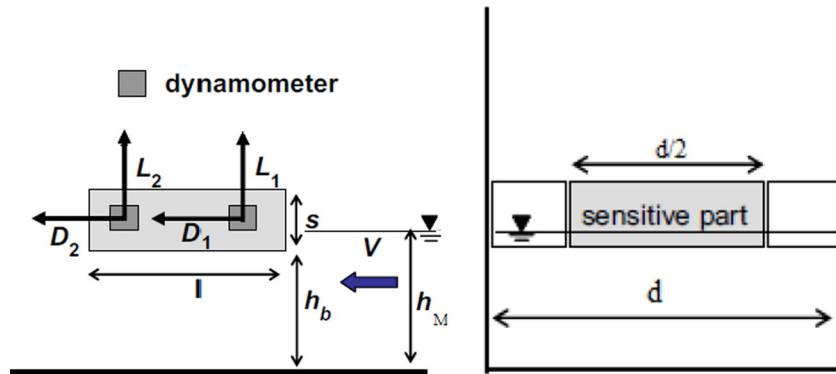


Fig. 7 Force measurement part of the physical model. Side view (left) and back view (right).

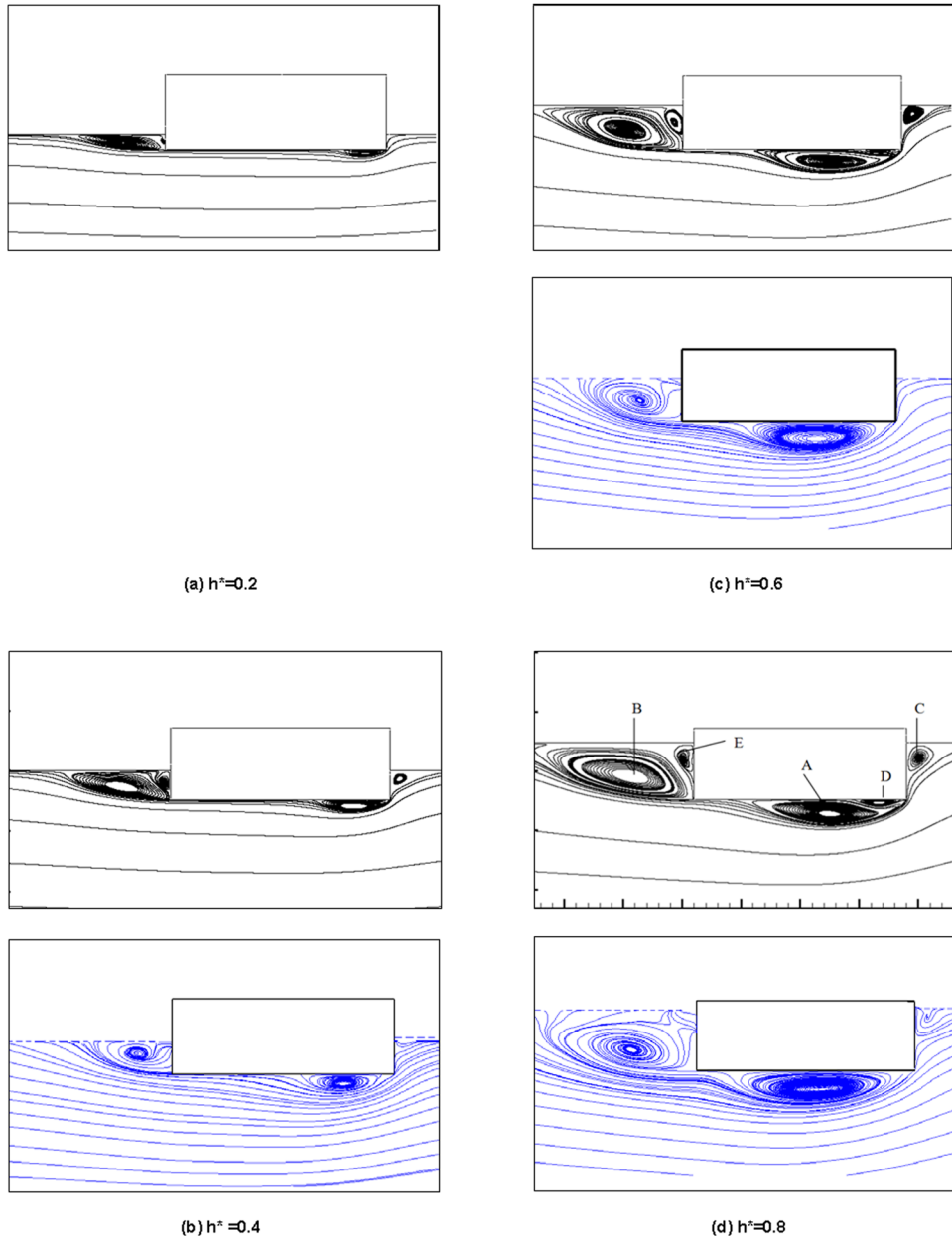


Fig. 8 Mean streamlines for different submergence ratios (h^*). The figures at the top with black lines are the CFD calculations and the blue lines at the bottom are from the PIV measurements (PIV data for $h^* = 0.2$ is not available).

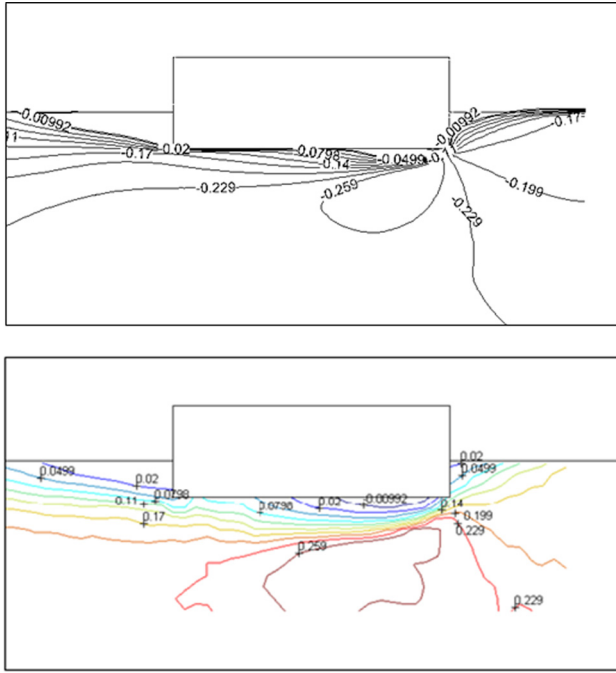


Fig. 9 Mean streamwise velocity. Calculated (top) and measured (bottom) for $h^* = 0.4$.

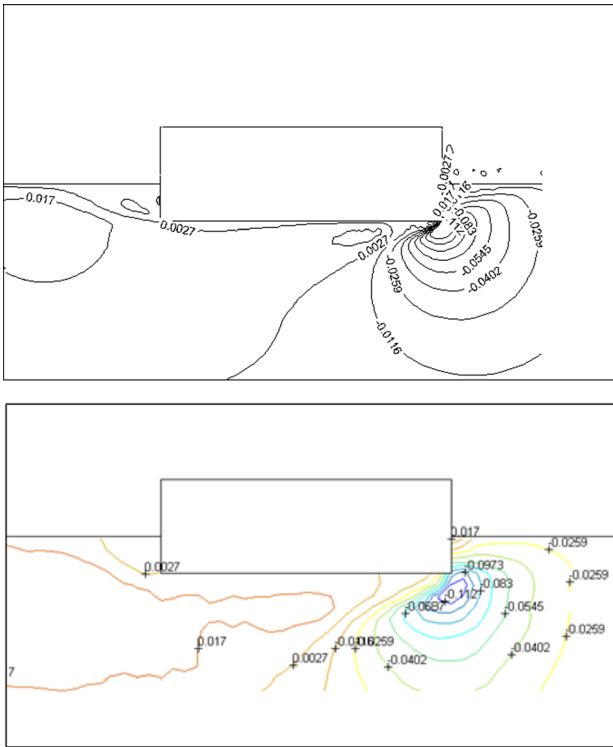
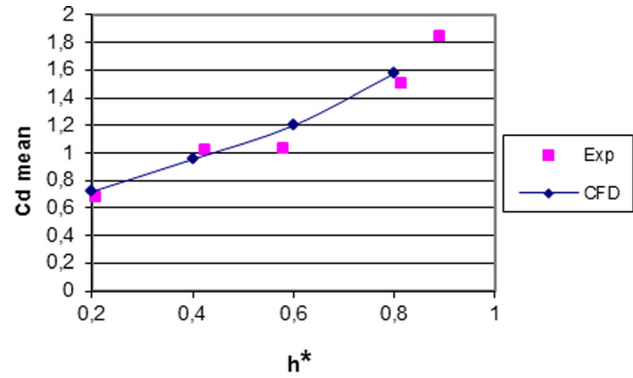


Fig. 10 Mean vertical velocity. Calculated (top) and measured (bottom) for $h^* = 0.4$.

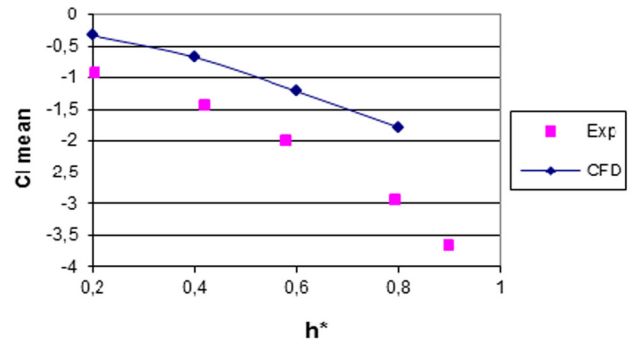
$$C_D = \frac{D_1 + D_2}{0.5\rho U_0^2 T(d/2)} \quad (8)$$

$$C_L = \frac{L_1 + L_2}{0.5\rho U_0^2 l(d/2)}$$

Here, D_i and L_i ($i = 1, 2$) are the drag and lift components of the loads acting on the i th dynamometer and $T = h_M - h_b$ is the draft



(a) Drag



(b) Lift

Fig. 11 (a) Predicted and measured drag and (b) buoyancy excluded lift force coefficients versus submergence ratios (h^*)

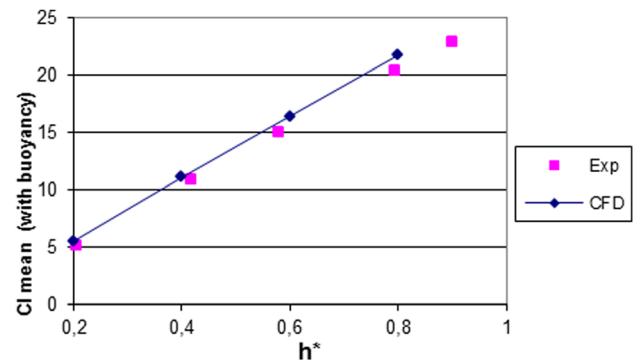
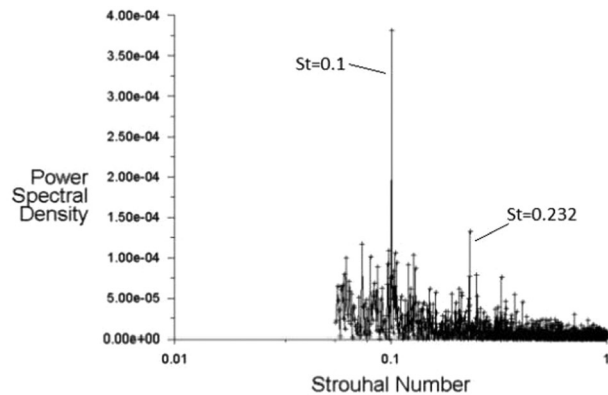


Fig. 12 Total lift force coefficient including buoyancy

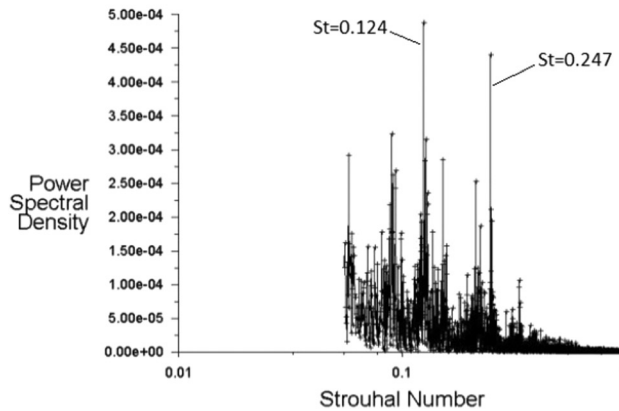
of the cylinder, as defined in the calculations. More details can be found in Ref. [39].

Results and Discussion

Simulations performed for $h^* = 0.2, 0.4, 0.6$, and 0.8 by using the computational grid MESH-1 and the effect of submergence on the flow field is studied. In Fig. 8, the calculated time- and spanwise-averaged flow field is compared with the PIV results for $h^* = 0.4, 0.6$, and 0.8 . The trend of the measured and predicted mean streamline profiles are in good agreement with each other. The flow is separated from the leading edge of the rectangular cylinder and reattached to the lower surface of the cylinder. The height of the primary bubble near the upstream (right) corner is



(a) $h^*=0.4$



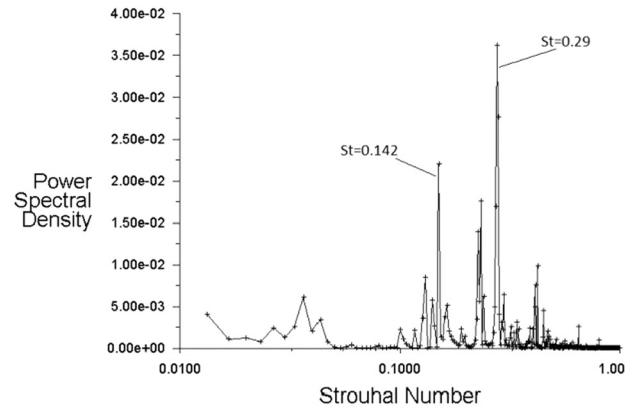
(b) $h^*=0.8$

Fig. 13 Power spectra of the lift coefficient for the experimental results for (a) $h^* = 0.4$, and (b) $h^* = 0.8$

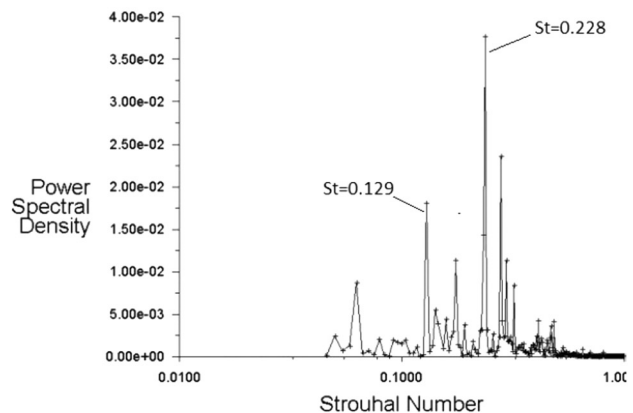
well predicted in the calculations. The reattachment length in the CFD simulations is slightly shorter than the PIV measurements. The shape and size of the separation near the downstream (left) corner are well predicted. The main separation bubble underneath the cylinder (A) and the main vortex structure in the wake (B) are shown in Fig. 8(d). There are also secondary separation bubbles at the leading edge of the cylinder (D) and in the leeward wake (E). Near the stagnation point, a smaller vortex (C) also occurred, except for $h^* = 0.2$, as shown in Fig. 8(a).

The separation process is related to submergence, even for the same Reynolds and Froude numbers. As the submergence ratio h^* increases, the height of the separation bubble (A) dramatically increases. The reattachment point also swaps backwards at higher h^* values. The size of the primary wake vortex (B) is also considerably affected by the submergence ratio. The size of the secondary separation bubble (D) is increasing with h^* , though it is very small for $h^* = 0.2$. The strength of the vortex (E) is getting larger for submergence ratios higher than 0.2 and stays almost constant for $h^* = 0.6$ and 0.8. Vortex (C) is not seen for $h^* = 0.2$ but for higher submergence ratios, its size does not change with h^* . In Figs. 9 and 10, the mean streamwise and normal velocity components are plotted based on both the calculations and measurements for $h^* = 0.4$. As seen in Fig. 9, although the trend of the calculated mean streamwise velocity contours agree with the PIV measurements, small differences are observed due to the slightly underestimated reattachment length. That is the reason why the vertical component of the mean velocity is also predicted to be slightly smaller than in the experiments (see Fig. 10).

Buoyancy forces are discarded from the lift coefficients when the vertical components of the forces are calculated for both the experiments and simulations. In Fig. 11, it is seen that the pre-



(a) $h^*=0.4$



(b) $h^*=0.8$

Fig. 14 Power spectra of the lift coefficients for the numerical results for (a) $h^* = 0.4$, and (b) $h^* = 0.8$

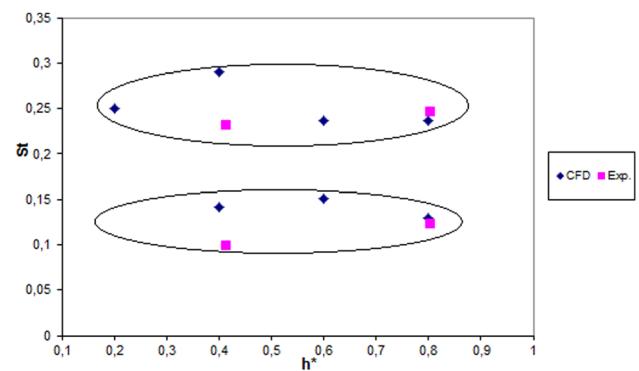


Fig. 15 Strouhal numbers for the numerical results

dicted mean drag coefficients (C_D) are in good agreement with the measurements for all submergence ratios. However, the lift coefficients (buoyancy excluded) are highly under-predicted (the minus sign of the lift coefficients shows that the force is acting downwards). The uncertainty related to the corresponding measurement for the lift forces is around 10%, which has been reported by Malavasi and Guadagnini [48].

The total lift force coefficient, including the lift and buoyancy forces, is plotted in Fig. 12. Since the lift force created by the flow

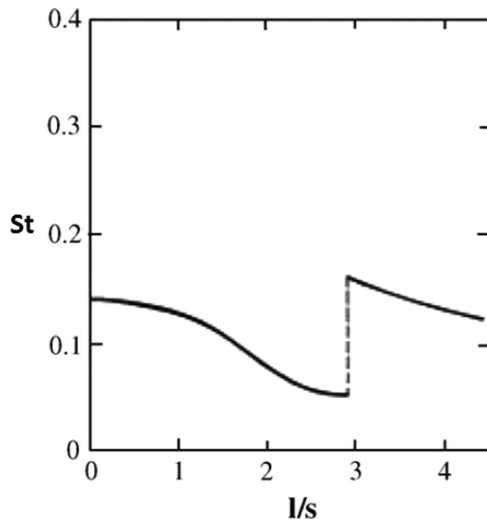
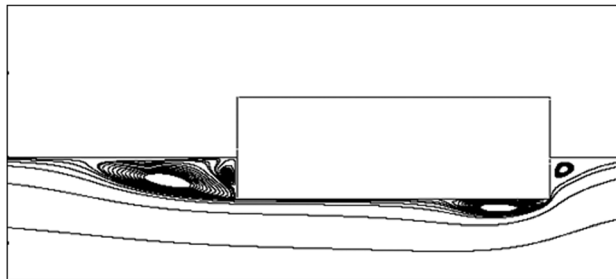
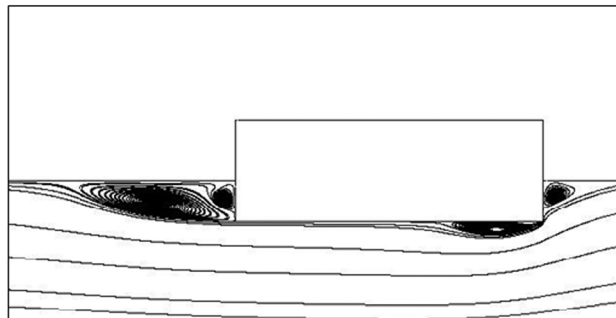


Fig. 16 Strouhal numbers as a function of the aspect ratio (l/s)



(a) MESH-1



(b) MESH-2

Fig. 17 Calculated mean streamlines for (a) MESH-1, and (b) MESH-2; $h^* = 0.4$

field is mainly due to the pressure distribution at the lower side of the cylinder and is small compared to the buoyancy component, the calculated total vertical force is very close to the measured data. That means that the inconsistency coming from the difference between measurements and calculations has no great role when the total vertical force is considered.

The frequency analysis by means of the FFT for the lift force coefficient has been performed on both the experimental and computational data. The Strouhal number ($St = fs/U_0$) is calculated based on the frequency (f) of the lift force. In Fig. 13, the power spectral densities are plotted for $h^* = 0.4$ and $h^* = 0.8$, based on experimental results. Two peak values have been seen as dominant Strouhal numbers. For the submergence ratios $h^* = 0.2$ and $h^* = 0.6$, there are no significant peaks in the frequencies of the

Table 2 Drag and total lift coefficients and Strouhal numbers for different meshes ($h^* = 0.4$ for simulations, $h^* = 0.424$ for the experiment)

Case number	Mesh (million)	Time-step (s)	$\overline{C_D}$	$\overline{C_L}$	St.1	St.2
MESH-1	1.9	0.001	0.96	33.3	0.14	0.29
MESH-2	4.5	0.001	0.90	33.4	0.15	0.27
MESH-3	9.0	0.001	1.10	33.2	0.13	0.32
MESH-4	20.0	0.0005	1.03	33.2	0.14	0.30
Exp.			1.02	34.3	0.10	0.23

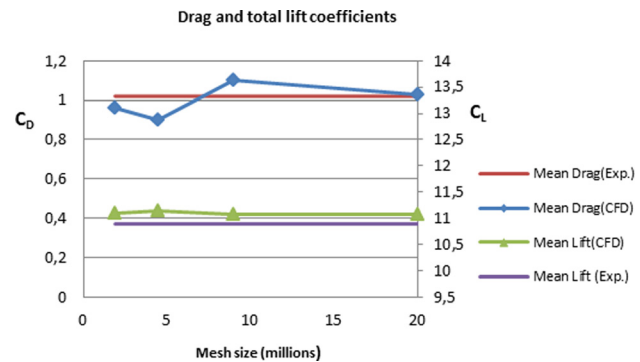


Fig. 18 Calculated mean drag and total lift coefficients versus mesh size, $h^* = 0.4$

lift coefficient because of the noisy data in the experiments. In the simulation results, the lower peak frequency is not seen very clearly and the higher frequency peak is more dominant, as can be seen in Fig. 14.

In Fig. 15, the Strouhal numbers of the lift coefficients for available h^* values are plotted, based on both the experimental and numerical results. The Strouhal numbers are scattered in the range of 0.23 to 0.28 for the higher frequency peak and 0.1 to 0.15 for the lower frequency peak in both the experimental and numerical simulations, as shown in the two ellipsoidal zones.

The previous works by Deniz and Staubli [3], Knisely [13], Nakamura and Yoshimura [7], Norberg [1], Okajima [12], and Shimada and Ishihara [23] clearly demonstrate that, for the flow around the rectangular cylinder, multiple shedding frequencies are recognizable in the range $2 < l/s < 3$. Based on these works, Fig. 16 illustrates the remarkable jump and double frequencies occurring at aspect ratio $l/s \sim 2-3$, which marks the limit between the flow regimes. These jumps are caused by transitions of the significant vortex formations. When l/s is close to 3, sporadic shedding occurs and it is difficult to observe distinct frequencies for this critical jump region. The same behavior is seen in the present work and the energy levels for two frequencies from the calculations, which are inverted in the experiments. Also additional peaks occurred in both the experiment and calculation. This might be due to sensitivity at this range of the l/s values. Shimada and Ishihara [23] showed that within a certain time range, the lower frequency component is predominant and at other time ranges the higher frequency is predominant. Small variation in the l/s value also change which frequency is becoming predominant. The inconsistency in the calculated Strouhal numbers might be an indicator of the difficulty of predicting the flow unsteadiness and instabilities for $l/s \sim 3$.

The simulations are repeated for finer meshes (MESH-2, MESH-3, and MESH-4) and the calculated mean streamlines are compared in Fig. 17 in order to check the grid dependency of the simulations. The size and shape of the vortex structures and reattachment mechanism are sufficiently close to each other. In Table 2, the total lift and drag coefficients and Strouhal numbers are tabulated for the different meshes. In Fig. 18, the calculated

Table 3 Drag and lift coefficients and Strouhal numbers ($h^* = 0.4$, MESH-1) for different time step sizes

Case number	Mesh (million)	Time-step (s)	$\overline{C_D}$	$\overline{C_L}$	St.1	St.2
MESH-1	1.9	0.0025	0.96	33.3	0.24	0.30
MESH-1	1.9	0.001	0.96	33.3	0.14	0.29
MESH-1	1.9	0.00025	1.05	33.2	0.13	0.29

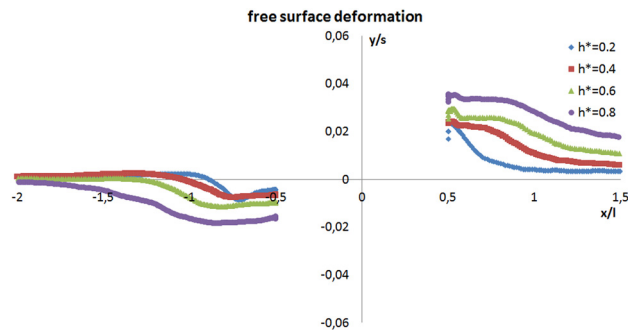


Fig. 19 Free surface deformation (numerical results)

mean of the total lift and drag coefficients are plotted versus the mesh size. The results are from MESH-1, MESH-2, MESH-3, and MESH-4. The straight line shows the experimental value. The deviation due to mesh resolution can be compared with the measurements in Fig. 18. In order to keep numerical stability, 0.0005 s is used for the time step size in the simulation with MESH-4.

The effect of the time step size on the results of the simulations is investigated by repeating the calculations with several time step sizes. The results are tabulated in Table 3. For the largest time step size, hydrodynamic force coefficients and the higher Strouhal number are predicted in the same range but the low frequency is off from the other results. The case with the smallest time step predicted both of the Strouhal numbers in the same range but the time step size affects the drag forces slightly. The drag force is predicted to be 9% higher than the one with larger time steps. However, the overall picture shows that the time step size 0.001 is sufficiently small to reproduce the time scales for the flow.

In the simulations, the free surface deformation has been calculated based on the volume fraction of water in the upwind side and wake of the cylinder. In Fig. 19, the free surface levels are plotted for different h^* values. The graph shows the water rise and drop near the cylinder dependent on s . The x axis shows the distance from the cylinder in the nondimensional form. As seen in Fig. 19, the free surface deformation is varying with the submergence ratio but the absolute quantities are very small compared to the height (s) of the cylinder. It varies between -0.02 s and 0.04 s.

Even though the water elevation is small, the effect of the free surface on the calculated hydrodynamic forces can be observed. The flow around a submerged rectangular cylinder with a 3:1 aspect ratio has been calculated with a different approach: the free

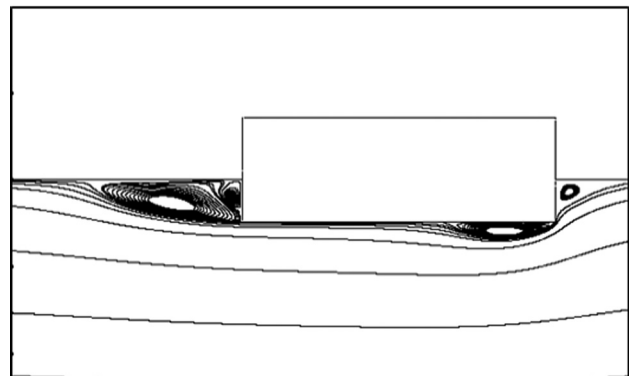
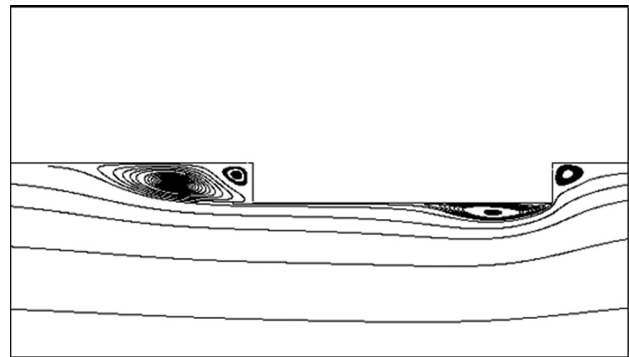


Fig. 20 Mean streamlines: free-slip boundary condition (top) and VOF method (bottom); $h^* = 0.4$

surface is modeled as a frictionless wall, which is the simple approximation used in several earlier works, especially for low Froude numbers. The numerical methods and parameters, turbulence model details, and solution grid type is the same, except for the modeling of the air side that has been done with a multiphase (VOF) approach. The mesh used in this simulation is referred to MESH-1a, which is created by eliminating the top air side of MESH-1. In Fig. 20, mean streamlines calculated by these two methods are compared. The mean separation bubble with the free-slip boundary condition (top) is slightly longer than the VOF results (bottom). The difference might be due to the small water elevation near the stagnation point and its effect on the main vortex at the upwind side of the flow and, indirectly, also by the separation mechanism at the leading corner. However, the calculated mean lift and drag forces are in good agreement. The drag and lift coefficients calculated by MESH-1 are 0.96 and 33.3, respectively, while with the free-slip boundary condition the estimated drag and total lift coefficients are 0.98 and 33.4, as shown in Table 4. The differences are 2% and 0.5%, respectively. This alternative method failed for estimating the Strouhal numbers. The small and large Strouhal number is 0.2 and 0.4, which is far from the ranges shown in Fig. 15. This might be due to differences in

Table 4 Drag and lift coefficients and Strouhal numbers ($h^* = 0.4$) for different boundary conditions at the side walls and mesh resolution in the spanwise direction

Case number	Mesh (million)	Time-step (s)		$\overline{C_D}$	$\overline{C_L}$	St.1	St.2
MESH-1	1.9	0.001		0.96	33.3	0.14	0.29
MESH-1a	1.4	0.001	Freeslip bc.	0.98	33.4	0.20	0.40
MESH-5	3.2	0.001	Side walls	0.98	33.5	0.15	0.29
MESH-6	3.8	0.001	Spanwise doubled	1.01	33.3	0.16	0.29

the separation mechanism near the upwind corner calculated with the free-slip boundary condition.

The side walls in the computational domain have periodic boundary conditions, as previously described. However, the experiments were done in a circulating water tunnel where the corresponding boundaries are solid walls. The effect of the slowing down of the flow due to friction at these walls is questionable. In order to see this effect, the simulations are repeated by modifying MESH-1 with the wall boundary conditions at the side walls. To solve the boundary layer near these walls, a structural mesh layer was added and the solution grid is referred to as MESH-5 with 3.2×10^6 elements. With this mesh, the drag coefficient is found to be 2% larger than the case with periodic conditions. The side walls do not considerably affect the lift. The Strouhal number appeared to be in the same range for this case, as shown in Table 4.

The effect of the mesh resolution in the spanwise direction is another question. In order to see this effect, simulations have been done with a grid which has twice the number of elements in the spanwise direction compared to MESH-1. This case is referred to as MESH-6, with 3.8×10^6 elements in total. The mesh topology in the xy plane is the same as for MESH-1. While changing the spanwise resolution affects the drag coefficient and lower Strouhal number (St.1) 5% and 13%, respectively, the higher Strouhal number (St.2) and the lift coefficient remain constant, as shown in Table 4.

Conclusions, Discussion, and Future Work

In this work, the flow around a sharp-edged rectangular cylinder at the free surface has been investigated. The hydrodynamic loads acting on the structure have been studied. It can be seen that the flow separation and reattachment mechanism at the submerged surface of the cylinder and the vortex formation in the wake behind it is highly affected by the submergence ratio, together with the free surface. Thus, the submergence ratio has a great influence on the size and shape of the separation bubble and the primary vortex in the wake.

The predicted drag forces are in good agreement with the measurements. Naturally, the drag forces increase with the submergence ratio. However, the lift forces are underestimated in the calculations compared to the measurements. The uncertainty is probably due to the complexity of the flow field underneath the rectangular section. The unsteadiness and complex vortex formation near the separation and reattachment points makes the inlet turbulence level important to the calculated pressure field in this region. The lift coefficients are predicted to be lower than the measurements (between 40–60%). The uncertainty in the lift forces for both the measurements and calculations have been reported in previous studies of flow around square and rectangular cylinders (Sohankar et al. [21], Mannini et al. [49], and Schewe [37]). The turbulence intensity at the inlet can influence the lift coefficient. A sensitivity analysis should be done for the inlet turbulence level. Nevertheless, the calculated lift forces due to the flow are approximately 6% of the total vertical forces, including buoyancy. Thus, the difference between the simulations and experiments, in terms of the total vertical force, is about 3%. This value is acceptable in engineering applications. For example, if the structure is floating instead of being fixed, the resulting change of draft due to the inconsistency for the vertical forces will be small enough to avoid the changes in the flow field and drag forces.

Even though the water rise near the stagnation point is very small, it is probably interacting with the small upstream vortex (C), (see Fig. 8(d)). However, the effect of this vortex to the separation at the upwind corner is a question. Therefore, the free surface may cause different vortex behaviors, especially for flows at higher Froude numbers. Simulations and experiments should be repeated for higher Froude numbers in order to explore these effects.

Acknowledgment

A Ph.D. research fellowship for the first author was provided by the Research Council of Norway. Computing time was granted by the Research Council of Norway via NOTUR (The Norwegian Metacenter for Computational Science).

References

- [1] Norberg, C., 1993, "Flow Around Rectangular Cylinders: Pressure Forces and Wake Frequencies," *J. Wind Eng. Ind. Aerodyn.*, **49**(1), pp. 187–196.
- [2] Awbi, H., 1983, "Effect of Blockage on the Strouhal Number of Two-Dimensional Bluff Bodies," *J. Wind Eng. Ind. Aerodyn.*, **12**(3), pp. 353–362.
- [3] Deniz, S., and Staubli, T., 1997, "Oscillating Rectangular and Octagonal Profiles: Interaction of Leading- and Trailing-Edge Vortex Formation," *J. Fluids Struct.*, **11**(1), pp. 3–31.
- [4] Kim, K. C., Ji, H. S., and Seong, S. H., 2003, "Flow Structure Around a 3-D Rectangular Prism in a Turbulent Boundary Layer," *J. Wind Eng. Ind. Aerodyn.*, **91**(5), pp. 653–669.
- [5] Matsumoto, M., Shirato, H., Araki, K., Haramura, T., and Hashimoto, T., 2003, "Spanwise Coherence Characteristics of Surface Pressure Field on 2-D Bluff Bodies," *J. Wind Eng. Ind. Aerodyn.*, **91**(1), pp. 155–163.
- [6] Mills, R., Sheridan, J., and Hourigan, K., 2002, "Response of Base Suction and Vortex Shedding From Rectangular Prisms to Transverse Forcing," *J. Fluid Mech.*, **461**, pp. 25–49.
- [7] Nakamura, Y., and Yoshimura, T., 1982, "Flutter and Vortex Excitation of Rectangular Prisms in Pure Torsion in Smooth and Turbulent Flows," *J. Sound Vib.*, **84**(3), pp. 305–317.
- [8] Shadaram, A., Fard, M. A., and Rostamy, N., 2008, "Experimental Study of Near Wake Flow Behind a Rectangular Cylinder," *J. Appl. Sci.*, **5**(8), pp. 917–926.
- [9] Nakamura, Y., and Ohya, Y., 1984, "The Effects of Turbulence on the Mean Flow Past Two-Dimensional Rectangular Cylinders," *J. Fluid Mech.*, **149**, pp. 255–273.
- [10] Nakaguchi, H., Hashimoto, K., and Muto, S., 1968, "An Experimental Study on Aerodynamic Drag of Rectangular Cylinders," *J. Jpn. Soc. Aeronaut. Space Sci.*, **16**(1), pp. 1–5.
- [11] Washizu, K., Ohya, A., Otsuki, Y., and Fujii, K., 1978, "Aeroelastic Instability of Rectangular Cylinders in a Heaving Mode," *J. Sound Vib.*, **59**(2), pp. 195–210.
- [12] Okajima, A., 1982, "Strouhal Numbers of Rectangular Cylinders," *J. Fluid Mech.*, **123**, pp. 379–398.
- [13] Knisely, C., 1990, "Strouhal Numbers of Rectangular Cylinders at Incidence: A Review and New Data," *J. Fluids Struct.*, **4**(4), pp. 371–393.
- [14] Bearman, P. W., and Trueman, D. M., 1972, "An Investigation of the Flow Around Rectangular Cylinders," *Aeronaut. Q.*, **23**, pp. 229–237.
- [15] Malavasi, S., and Blois, G., 2012, "Wall Effects on the Flow Structure Around a Rectangular Cylinder," *Meccanica*, **47**(4), pp. 805–815.
- [16] Hemon, P., and Santi, F., 2002, "On the Aeroelastic Behaviour of Rectangular Cylinders in Cross-Flow," *J. Fluids Struct.*, **16**(7), pp. 855–889.
- [17] Kuroda, K., Tamura, T., and Suzuki, M., 2007, "Applicability of LES to the Turbulent Wake of a Rectangular Cylinder—Comparison With PIV Data," *J. Wind Eng. Ind. Aerodyn.*, **95**(9), pp. 1242–1258.
- [18] Davis, R., and Moore, E., 1982, "A Numerical Study of Vortex Shedding From Rectangles," *J. Fluid Mech.*, **116**(3), pp. 475–506.
- [19] Kondo, N., and Yamada, S., 1995, "Third-Order Upwind Finite Element Computation of the Incompressible Navier-Stokes Equations—Part I. Computation of Flow around Rectangular Cylinders," *Comput. Methods Appl. Mech. Eng.*, **127**(1), pp. 87–97.
- [20] Ohya, Y., Nakamura, Y., Ozono, S., Tsuruta, H., and Nayakama, R., 1992, "A Numerical Study of Vortex Shedding From Flat Plates With Square Leading and Trailing Edges," *J. Fluid Mech.*, **236**, pp. 445–460.
- [21] Sohankar, A., Norberg, C., and Davidson, L., 1997, "Numerical Simulation of Unsteady Low-Reynolds Number Flow Around Rectangular Cylinders at Incidence," *J. Wind Eng. Ind. Aerodyn.*, **69**, pp. 189–201.
- [22] Yu, D., and Kareem, A., 1998, "Parametric Study of Flow Around Rectangular Prisms Using LES," *J. Wind Eng. Ind. Aerodyn.*, **77–78**, pp. 653–662.
- [23] Shimada, K., and Ishihara, T., 2002, "Application of a Modified K-E Model to the Prediction of Aerodynamic Characteristics of Rectangular Cross-Section Cylinders," *J. Fluids Struct.*, **16**(4), pp. 465–485.
- [24] Nakamura, Y., Ohya, Y., Ozono, S., and Nakayama, R., 1996, "Experimental and Numerical Analysis of Vortex Shedding From Elongated Rectangular Cylinders at Low Reynolds Numbers 200–103," *J. Wind Eng. Ind. Aerodyn.*, **65**(1–3), pp. 301–308.
- [25] Tamura, T., and Ito, Y., 1996, "Aerodynamic Characteristics and Flow Structures Around a Rectangular Cylinder With a Section of Various Depth/Breadth Ratios," *J. Struct. Constr. Eng.*, **486**, pp. 153–162.
- [26] Hirano, H., Watanabe, S., Maruoka, A., and Ikenouchi, M., 1999, "Aerodynamic Characteristics of Rectangular Cylinders," *Int. J. Comput. Fluid Dyn.*, **12**(2), pp. 151–163.
- [27] Krajnovic, S., and Davidson, L., "Flow Around a Three-Dimensional Bluff Body," Proceedings of the 9th International Symposium on Flow Visualisation, Heriot-Watt University, Edinburgh, pp. 1–9.
- [28] Lam, K., Lin, Y., Zou, L., and Liu, Y., 2012, "Numerical Study of Flow Patterns and Force Characteristics for Square and Rectangular Cylinders With Wavy Surfaces," *J. Fluids Struct.*, **28**, pp. 359–377.

- [29] Sohankar, A., 2008, "Large Eddy Simulation of Flow Past Rectangular-Section Cylinders: Side Ratio Effects," *J. Wind Eng. Ind. Aerodyn.*, **96**(5), pp. 640–655.
- [30] Almeida, O., Mansur, S., and Silveira-Neto, A., 2008, "On the Flow Past Rectangular Cylinders: Physical Aspects and Numerical Simulation," *Therm. Eng.*, **7**(1), pp. 55–64. Available at: http://demec.ufpr.br/term/ed_ant/13/artigo/ciencia/9-149.pdf.
- [31] Noda, H., and Nakayama, A., 2003, "Reproducibility of Flow Past Two-Dimensional Rectangular Cylinders in a Homogeneous Turbulent Flow by LES," *J. Wind Eng. Ind. Aerodyn.*, **91**(1), pp. 265–278.
- [32] Arslan, T., Khoury, G. K. E., Pettersen, B., and Andersson, H. I., "Simulations of Flow Around a Three-Dimensional Square Cylinder Using LES and DNS," Proceedings of the Seventh International Colloquium on Bluff Bodies Aerodynamics and Applications, Shanghai, China, pp. 909–918.
- [33] Bartoli, G., Bruno, L., Buresti, G., Ricciardelli, F., Salvetti, M. V., and Zasso, A., 2008, "BARC Overview Document," <http://www.aniv-iawe.org/barc>
- [34] Bruno, L., Fransos, D., Coste, N., and Bosco, A., 2010, "3D Flow Around a Rectangular Cylinder: A Computational Study," *J. Wind Eng. Ind. Aerodyn.*, **98**(6–7), pp. 263–276.
- [35] Mannini, C., and Schewe, G., "Numerical Study on the Three-Dimensional Unsteady Flow Past a 5:1 Rectangular Cylinder Using the DES Approach," Proceedings of the Thirteenth International Conference on Wind Engineering, Amsterdam, The Netherlands, pp. 511–518.
- [36] Schewe, G., "Influence of the Reynolds-Number on Flow-Induced Vibrations of Generic Bridge Sections," Proceedings of the Bridges International Conference, Dubrovnik, Croatia, pp. 351–358.
- [37] Schewe, G., "Reynolds Number Effects in Flow Around a Rectangular Cylinder With Aspect Ratio 1:5," Proceedings of the Fifth European and African Conference on Wind Engineering, Florence, Italy.
- [38] Arslan, T., Pettersen, B., and Andersson, H. I., "Calculations of the Flow Around Rectangular Shaped Floating Structures," Proceedings of the Thirteenth International Conference on Wind Engineering, Amsterdam, The Netherlands, pp. 523–530.
- [39] Malavasi, S., and Guadagnini, A., 2007, "Interactions Between a Rectangular Cylinder and a Free-Surface Flow," *J. Fluids Struct.*, **23**(8), pp. 1137–1148.
- [40] Malavasi, S., Franzetti, S., and Blois, G., "PIV Investigation of Flow Around Submerged River Bridge Deck," Proceedings of the International Conference of River Flows, Napoli, Italy, pp. 601–608.
- [41] Malavasi, S., and Blois, G., 2007, "Influence of the Free Surface on the Flow Pattern Around a Rectangular Cylinder," Ninth International Symposium on Fluid Control, Measurements and Visualization, Tallahassee, FL.
- [42] Ting, F. C. K., and Kim, Y.-K., 1994, "Vortex Generation in Water Waves Propagating Over a Submerged Obstacle," *Coastal Eng.*, **24**(1–2), pp. 23–49.
- [43] Smagorinsky, J., 1963, "General Circulation Experiments With the Primitive Equations," *Mon. Weather Rev.*, **91**(3), pp. 99–164.
- [44] Germano, M., Piomelli, U., Moin, P., and Cabot, W. H., 1991, "A Dynamic Subgrid-Scale Eddy Viscosity Model," *Phys. Fluids A*, **3**, p. 1760.
- [45] Hirt, C. W., and Nichols, B. D., 1981, "Volume of Fluid (VOF) Method for the Dynamics of Free Boundaries," *J. Comput. Phys.*, **39**(1), pp. 201–225.
- [46] Muzafherija, S., Peric, M., Sames, P., and Schellin, T., "A Two-Fluid Navier-Stokes Solver to Simulate Water Entry," Proceedings of the 22nd Symposium on Naval Hydrodynamics, Washington, D.C., pp. 277–289.
- [47] Kim, S., 2004, "Large Eddy Simulation Using Unstructured Meshes and Dynamic Subgrid-Scale Turbulence Models," AIAA Paper No. 2548.
- [48] Malavasi, S., and Guadagnini, A., 2003, "Hydrodynamic Loading on River Bridges," *J. Hydraul. Eng.*, **129**(11), pp. 854–861.
- [49] Mannini, C., Weinman, K., Soda, A., and Schewe, G., "Three-Dimensional Numerical Simulation of Flow Around a 1: 5 Rectangular Cylinder," Proceedings of the 5th European and African Conference on Wind Engineering, Florence, Italy.